

Highlights

- Neural trajectories in the hippocampus exhibited greater variability during a working memory (WM) task compared to those in the entorhinal cortex and amygdala regions.
- The distance of neural trajectories between encoding and retrieval states in the hippocampus was memory-load dependent during a WM task.
- Hippocampal neural trajectories fluctuated between the encoding and retrieval states in a task-dependent manner during both baseline and sharp-wave ripple (SWR) periods.
- Hippocampal neural trajectories shifted from encoding to retrieval states during SWR period.

Hippocampal Neural Fluctuations Between Memory Encoding and Retrieval States During a Working Memory Task in Humans

Yusuke Watanabe^{a,*}, Yuji Ikegaya^{b,c,d}, Takafumi Yanagisawa^{a,e}

^a*Institute for Advanced Cocreation studies, Osaka University, 2-2 Yamadaoka, Suita, 565-0871, Osaka, Japan*

^b*Graduate School of Pharmaceutical Sciences, The University of Tokyo, 7-3-1 Hongo, Tokyo, 113-0033, Japan*

^c*Institute for AI and Beyond, The University of Tokyo, 7-3-1 Hongo, Tokyo, 113-0033, Japan*

^d*Center for Information and Neural Networks, National Institute of Information and Communications Technology, 1-4 Yamadaoka, Suita City, 565-0871, Osaka, Japan*

^e*Department of Neurosurgery, Osaka University Graduate School of Medicine, 2-2 Yamadaoka, Osaka, 565-0871, Japan*

Abstract

Working memory (WM) is crucial for a multitude of cognitive functions, but its underlying neural mechanisms at play remain to be fully understood. Interestingly, the hippocampus and sharp-wave ripples (SWRs)— transient and synchronous oscillation observed in the hippocampus — garner recognition for their significance in memory consolidation and retrieval, albeit their correlation with WM tasks remains to be elucidated. Here we show that during a WM task, multi-unit activity patterns in the hippocampus display distinctive dynamics, especially during SWR periods. This study analyzed intracranial electroencephalography data from the medial temporal lobe (MTL) of nine patients with epilepsy, recorded during an eight-second Sternberg task. Utilizing Gaussian-process factor analysis, we extracted low-dimensional neural representations or trajectories (NT) within MTL regions

*Corresponding author. Tel: +81-6-6879-3652 Email: ywatanabe@alumni.u-tokyo.ac.jp

during the Sternberg WM task. The results revealed significant variations in NT of the hippocampus compared to those of the entorhinal cortex and the amygdala. Additionally, the distance of the NT between the encoding and retrieval phases was dependent on memory load. Crucially, hippocampal NT oscillated during the retrieval phase between encoding and retrieval states in a task-dependent manner. Notably, these fluctuations shifted from encoding to retrieval states during SWR episodes. These findings reaffirm the role of the hippocampus in WM tasks and propose a hypothesis: the hippocampus transitions its functional state from encoding to retrieval during SWRs in WM tasks.

Keywords: working memory, memory load, hippocampus, sharp-wave ripples, humans

8 figures, 3 tables, 221 words for abstract, and 3082 words for main text

1. Introduction

Working memory (WM), serving as a key player in cognitive abilities, underpins our daily activities and relations with the world, from basic perceptual decision making to sophisticated cognitive operations. One remarkable component in the neural mechanisms of WM is the hippocampus, an area identified as being crucial for various forms of memory [1, 2, 3, 4, 5, 6, 7, 8, 9]. Unraveling the role and contributions of the hippocampus within the realm of working memory informs our understanding of the cognitive dynamics underpinning everyday functionality. This knowledge may ultimately foster the enhancement of cognitive performance and the development of interventions for memory-related disorders.

During working memory tasks, hippocampal networks yield transient, synchronized oscillations known as sharp-wave ripples (SWRs), which have been found to replay sequences of recent and prospective memory traces [10, 11, 12, 13]. Moreover, functional correlations between awake SWRs and

working memory performance over multi-day scales have been elucidated by selective SWR suppressions [14, 15, 16], and prolongation events [17], as well as functional lesioning in the dentate gyrus, a subregion of the hippocampus [18]. Certain studies have emphasized the coordination of SWRs with other oscillation components in the facilitation of working memory processing [19, 20]. Furthermore, SWR events that occur seconds before memory recall proffer a notion of their essentiality for effective execution of working memory tasks [21, 22, 23]. Despite these preliminary insights, our comprehensive understanding of SWRs and their temporal relationship with working memory processes remains largely incomplete.

One noteworthy limitation in the current body of research is predicated on the use of rodent navigation tasks, wherein the temporal attributes of the task were not sufficiently granular to discern the exact timings of memory acquisition, retrieval, and decision-making processes. Furthermore, the detection of SWRs during predominantly immobile periods in rodents [10, 11, 12, 13, 15, 16, 17], likely due to potential contamination from electromyographic noise [24], limits the extrapolation of experimental findings to subjectively equivalent functionality of WM in humans. It is thus imperative to explore the relationship between SWRs and human WM in a noise-controlled experimental setup with a temporally precise measurement of WM events.

The present study hypothesizes that human hippocampal neurons embody low-dimensional neural trajectories (NTs) that vary with WM load, particularly during SWR periods. To test this proposition, a human WM dataset with high temporal resolution (1 s for fixation, 2 s for encoding, 3 s for maintenance, and 2 s for retrieval) [25], capturing key phases of the WM circuit, was utilized.

To aptly analyze low-dimensional dynamics, dimensionality reduction techniques were implemented. Interestingly, recent findings have shown the presence of dynamic, nonlinear low-dimensional spaces within the firing patterns of hippocampal [26] and entorhinal cortex neurons in rodents [27]. Accordingly, we applied Gaussian-process factor analysis (GPFA), a proven

methodology for neural population dynamics analyses [28, 29, 30, 31, 32, 33, 34, 35, 36], on intracranial electroencephalography (iEEG) signals recorded from the medial temporal lobe, including the hippocampus, of patients performing a structured WM task.

2. Methods

2.1. Dataset

The dataset used in this study, which is publicly available, comprises nine epilepsy patients performing a modified the Sternberg task [25]. This task includes four phases: fixation (1s), encoding (2s), maintenance (3s), and retrieval (2s). During the encoding phase, participants were presented with a set of four, six, or eight alphabet letters. They were then tasked with determining whether a probe letter displayed during the retrieval phase had previously appeared (the correct response for Match IN task) or not (the correct response for Mismatch OUT task). Intracranial electroencephalography (iEEG) signals were captured with a 32 kHz sampling rate within a 0.5–5,000 Hz frequency range, using depth electrodes in the MTL regions: the anterior head of the left and right hippocampus (AHL and AHR), the posterior body of the hippocampus (PHL and PHR), the entorhinal cortex (ECL and ECR), and the amygdala (AL and AR), as depicted in Figure 1A and Table 1. The iEEG signals were subsequently downsampled to 2 kHz. Correlations between variables such as set size and correct rate were examined (Figure ??S1). Multiunit spike timing was determined via a spike sorting algorithm [37] using the Combinato package (<https://github.com/jniediek/combinato>) (Figure 1C).

2.2. Calculation of NT using GPFA

NTs, also referred to as 'factors', in the hippocampus, EC, and amygdala were determined using GPFA [28] applied to the multi-unit activity data for each session, performed with the elephant package (<https://readthedocs.io/en/latest/reference/gpfa.html>). The bin size was set

to 50 ms, without overlaps. Each factor was z-normalized across all sessions, and the Euclidean distance from the origin (O) was then computed.

For each NT within a region such as AHL, geometric medians (g_F for fixation, g_E for encoding, g_M for maintenance, and g_R for retrieval phase) were calculated by determining the median coordinates of the NT during the four phases. An optimal GPFA dimensionality was found to be three using the elbow method obtained by examining the log-likelihood values through a three-fold cross-validation approach (Figure 2B).

2.3. Identifying SWR candidates from hippocampal regions

Potential SWR events within the hippocampus were detected using a widely used method [38]. LFP signals from a region of interest (ROI) like AHL, were re-referenced by deducting the averaged signal from locations outside the ROI (for instance, AHR, PHL, PHR, ECL, ECR, AL, and AR). The re-referenced LFP signals were then filtered with a ripple-band filter (80–140 Hz) to determine SWR candidates, marked as SWR^+ candidates. SWR detection was carried out using a published tool (https://github.com/Eden-Kramer-Lab/ripple_detection) [39], with the bandpass range adjusted to 80–140 Hz for humans [22, 23, 38], unlike the original 150–250 Hz range typically applied to rodents [40].

Control events for SWR^+ candidates, labeled as SWR^- candidates, were detected by randomly shuffling the timestamps of SWR^+ candidates across all trials and subjects. The resulting $\text{SWR}^+/\text{SWR}^-$ candidates were then visually inspected.

2.4. Defining SWRs from Putative Hippocampal CA1 Regions Using UMAP Clustering

Potential SWRs were differentiated from SWR candidates in putative CA1 (cornu Ammonis 1) regions. The definition of putative CA1 regions was as follows. First, SWR^+ and SWR^- candidates in the hippocampus were projected into a two-dimensional space using a supervised clustering method,

Uniform Manifold Approximation and Projection (UMAP) [41]. The input features for this projection were the spike counts per unit during the period of SWR^+ or SWR^- candidates. Clustering validation was performed by calculating the silhouette score [42] from clustered sample points in the corresponding two-dimensional space. Regions in the hippocampus that scored above 0.6 on average across sessions (75^{th} percentile) were identified as putative CA1 regions. This process resulted in the identification of five electrode positions from five patients.

$\text{SWR}^+/\text{SWR}^-$ candidates in these predetermined CA1 regions were categorized as $\text{SWR}^+/\text{SWR}^-$, and thus they no longer retained their candidate status. The duration and ripple band peak amplitude of SWRs were found to follow log-normal distributions. Each time period of SWR was partitioned relative to the time from the SWR center into pre- (at -800 ms to -300 ms from the SWR center), mid- (at -250 to $+250$ ms), and post-SWR (at $+300$ to $+800$ ms) times.

2.5. Statistical Evaluation

Both the Brunner–Munzel test and the Kruskal-Wallis test were executed using the SciPy package in Python [43]. Correlational analysis was conducted by determining the rank of the observed correlation coefficient within its associated set-size-shuffled surrogate using a customized Python script. The bootstrap test was implemented with an in-house Python script.

3. Results

3.1. *iEEG Recording and NT in MTL Regions during the Sternberg Task*

Our analysis employed a publicly accessible dataset [25], which comprises LFP signals (Figure 1A) from MTL regions (Table 1) recorded during the execution of the modified Sternberg task. We extracted SWR^+ candidates from LFP signals that were filtered in the 80–140 Hz ripple band (Figure 1B),

originating in all hippocampal regions (refer to Methods section). Meanwhile, SWR⁻ candidates, control events for SWR⁺ candidates, were defined at the same timestamps but distributed across different trials (Figure 1). The dataset encompassed multi-unit spikes (Figure 1C), recognized via a spike sorting algorithm [37]. Employing GPFA [28], we applied this to 50-ms windows of binned multi-unit activity without overlaps to determine the NTs, or factors, of MTL regions by session and region (Figure 1D). We normalized each factor per session and region, for instance, session #2 in AHL of subject #1. We then calculated the Euclidean distance from the origin (O) (Figure 1E).

3.2. Correlation of Hippocampal NT with the Sternberg Task

Figure 2A exhibits a distribution of median NTs, comprising 50 trials, within the three main factor spaces. Utilizing the elbow method, we established the optimal embedding dimension for the GPFA model as three (Figure 2B). The NT distance from the origin (O) — represented as $\|g_F\|$, $\|g_E\|$, $\|g_M\|$, and $\|g_R\|$ — in the hippocampus surpassed the corresponding distances in the EC and amygdala (Figure 2C & D).¹

Similarly, we computed the distances between the geometric medians of four phases, namely $\|g_{Fg_E}\|$, $\|g_{Fg_M}\|$, $\|g_{Fg_R}\|$, $\|g_{Eg_M}\|$, $\|g_{Eg_R}\|$, and $\|g_{Mg_R}\|$. The hippocampus showed larger distances between phases than those in the EC and amygdala.²

¹Hippocampus: Distance = 1.11 [1.01], median [IQR], $n = 195,681$ timepoints; EC: Distance = 0.94 [1.10], median [IQR], $n = 133,761$ timepoints; Amygdala: Distance = 0.78 [0.88], median [IQR], $n = 165,281$ timepoints.

²Hippocampus: Distance = 0.60 [0.70], median [IQR], $n = 8,772$ combinations; EC: Distance = 0.28 [0.52], median [IQR], $n = 5,017$ combinations ($p < 0.01$; Brunner–Munzel test); Amygdala: Distance = 0.24 [0.42], median [IQR], $n = 7,466$ combinations ($p < 0.01$; Brunner–Munzel test).

3.3. Memory-Load-Dependent NT Distance between Encoding and Retrieval States in the Hippocampus

Regarding memory load in the Sternberg task, we observed a negative correlation between the correct rate of trials and the set size, which denotes the number of letters to be encoded (Figure 3A).³ Concomitantly, a positive correlation was noted between the response time and set size (Figure 3B).⁴.

Next, we discovered a positive correlation between set size and the NT distance separating the encoding and retrieval phases ($\log_{10}\|\mathbf{g}_{\text{EGR}}\|$) (Figure 3C).⁵. However, distances between other phase combinations did not highlight statistically significant correlations (Figures 3D and ??).

3.4. Detection of Hippocampal SWRs from Putative CA1 Regions

To enhance the precision of recording sites and SWR detection, we approximated the electrode placements in the CA1 regions of the hippocampus using distinguished multi-unit spike patterns during SWR events. SWR⁺/SWR⁻ candidates from each session and hippocampal region were embedded in two-dimensional space using UMAP (Figure 4A).⁶ With the silhouette score as a quality metric for clustering (Figure 4B and Table 2), recording sites demonstrating an average silhouette score exceeding 0.6 across all sessions were

³Correct rate: set size four (0.99 ± 0.11 , mean \pm SD; $n = 333$ trials) vs. set size six (0.93 ± 0.26 ; $n = 278$ trials; $p < 0.001$, Brunner–Munzel test with Bonferroni correction) and set size eight (0.87 ± 0.34 ; $n = 275$ trials; $p < 0.05$; Brunner–Munzel test with Bonferroni correction). Generally, $p < 0.001$ for Kruskal–Wallis test; correlation coefficient = - 0.20, $p < 0.001$.

⁴Response time: set size four (1.26 ± 0.45 s; $n = 333$ trials) vs. set size six (1.53 ± 0.91 s; $n = 278$ trials) and set size eight (1.66 ± 0.80 s; $n = 275$ trials). All comparisons $p < 0.001$, Brunner–Munzel test with Bonferroni correction; $p < 0.001$ for Kruskal–Wallis test; correlation coefficient = 0.22, $p < 0.001$.

⁵Correlation between set size and $\log_{10}(\|\mathbf{g}_{\text{EGR}}\|)$: correlation coefficient = 0.05, $p < 0.001$. Specific values: $\|\mathbf{g}_{\text{EGR}}\| = 0.54$ [0.70] for set size four, $n = 447$; $\|\mathbf{g}_{\text{EGR}}\| = 0.58$ [0.66] for set size six, $n = 381$; $\|\mathbf{g}_{\text{EGR}}\| = 0.61$ [0.63] for set size eight, $n = 395$.

⁶Consider the AHL in session #1 of subject #1 as a case in point.

identified as putative CA1 regions.⁷ (Tables 2 and 3). We identified five putative CA1 regions, four of which were not indicated as seizure onset zones (Table 1).

Subsequently, SWR⁺/SWR⁻ candidates within these putative CA1 regions were labeled as SWR⁺ and SWR⁻, respectively⁸ (Table 3). Both SWR⁺ and SWR⁻ manifested identical durations⁹ due to their definitions and followed a log-normal distribution (Figure 4C). During the initial 400 ms of the retrieval phase, an increase in SWR⁺ incidence was found¹⁰ (Figure 4D). The peak ripple band amplitude of SWR⁺ surpassed that of SWR⁻ and followed a log-normal distribution (Figure 4E).¹¹

3.5. Transient Change in Hippocampal NT during SWR

We assessed the 'distance' of the NT from the origin (O) during SWR events in both encoding and retrieval phases (Figure 5A). Observing the increase in distance during SWR, as illustrated in Figure 5A, we categorized each SWR into three stages: pre-, mid-, and post-SWR. Hence, the distances from the origin O during those SWR intervals are identified as $\|\text{pre-eSWR}^+\|$, $\|\text{mid-eSWR}^+\|$ and others.

As a result, $\|\text{mid-eSWR}^+\|^{12}$ exceeded $\|\text{pre-eSWR}^+\|^{13}$, and $\|\text{mid-rSWR}^+\|^{14}$

⁷The identified regions were the AHL of subject #1, AHR of subject #3, PHL of subject #4, AHL of subject #6, and AHR of subject #9.

⁸These definitions produced equal counts for both categories: SWR⁺ ($n = 1,170$) and SWR⁻ ($n = 1,170$).

⁹These definitions result in equal durations for both categories: SWR⁺ (93.0 [65.4] ms) and SWR⁻ (93.0 [65.4] ms).

¹⁰SWR⁺ increased against the bootstrap sample; 95th percentile = 0.42 [Hz]; $p < 0.05$.

¹¹SWR⁺ (3.05 [0.85] SD of baseline, median [IQR]; $n = 1,170$) vs. SWR⁻ (2.37 [0.33] SD of baseline, median [IQR]; $n = 1,170$; $p < 0.001$; Brunner–Munzel test).

¹²1.25 [1.30], median [IQR], $n = 1,281$ in Match IN task; 1.12 [1.35], median [IQR], $n = 1,163$ in Mismatch OUT task

¹³1.08 [1.07], median [IQR], $n = 1,149$ in Match IN task; 0.90 [1.12], median [IQR], $n = 1,088$ in Mismatch OUT task

¹⁴1.32 [1.24], median [IQR], $n = 935$ in Match IN task; 1.15 [1.26], median [IQR], $n = 891$ in Mismatch OUT task

was larger than $\|\text{pre-rSWR}^+\|$ in both the Match IN and Mismatch OUT tasks.¹⁵.

3.6. Fluctuations of Hippocampal NTs between Encoding and Retrieval States

Subsequently, we investigated the 'direction' of the NT in relation to $\overrightarrow{\text{geg}_R}$, which was found to be dependent on memory load (Figure 3). The directions of the SWRs were determined by the NT at -250 ms and +250 ms from their center, denoted as, for example, $\overrightarrow{\text{eSWR}^+}$. We calculated the cosine similarities between $\overrightarrow{\text{geg}_R}$, $\overrightarrow{\text{eSWR}}$, and $\overrightarrow{\text{rSWR}}$ in both SWR (SWR⁺) and baseline periods (SWR⁻) (Figure 6A–D).

$\overrightarrow{\text{rSWR}^- \cdot \text{geg}_R}$ exhibited a biphasic distribution. By computing the difference between the distribution of $\overrightarrow{\text{rSWR}^+ \cdot \text{geg}_R}$ (Figure 6A & B) and that of $\overrightarrow{\text{rSWR}^- \cdot \text{geg}_R}$ (Figure 6C & D), we were able to determine the contributions of SWR (Figure 6E & F), which indicated a shift in the direction of $\overrightarrow{\text{geg}_R}$ (Figure 6E & F: *red rectangles*).

Furthermore, $\overrightarrow{\text{eSWR}^+ \cdot \text{rSWR}^+}$ was less than $\overrightarrow{\text{eSWR}^- \cdot \text{rSWR}^-}$ strictly in Mismatch OUT task (Figure 6F: *pink circles*). In other words, eSWR and rSWR pointed in the opposite direction exclusively in Mismatch OUT task but not Match IN task (Figure 6E: *pink circles*).

4. Discussion

This study hypothesizes that in low-dimensional spaces during a WM task in humans, hippocampal neurons exhibit WM-task dependent NTs, primarily during SWR periods. Initially, multi-unit spikes in the MTL regions were projected onto three-dimensional spaces during a Sternberg task using GPFA (Figure 1D–E & Figure 2A). The NT distances across WM phases ($\|\text{g}_{\text{FGE}}\|$, $\|\text{g}_{\text{FGM}}\|$, $\|\text{g}_{\text{FGR}}\|$, $\|\text{g}_{\text{EGM}}\|$, $\|\text{g}_{\text{EGR}}\|$, and $\|\text{g}_{\text{MGR}}\|$) were significantly larger in the hippocampus compared to the EC and amygdala (Figure 2C–E). Also,

¹⁵1.19 [0.96], median [IQR], $n = 673$ in Match IN task; 0.94 [0.88], median [IQR], $n = 664$ in Mismatch OUT task

in the hippocampus, the NT distance between the encoding and retrieval phases ($\|g_{GE}\|$) positively correlated with memory load (Figure 3C–D). The hippocampal NT transiently expanded during SWRs (Figure 5). Lastly, the hippocampal NT alternated between encoding and retrieval states, transitioning from encoding to retrieval during SWR events (Figure 6). These findings explain aspects of hippocampal neural activity during a WM task in humans and offer new insights into SWRs as a state-switching element in hippocampal neural states.

The longer disntace of NTs across the four phases in the hippocampus indicates dynamic and responsive neural activity in the hippocampus during the WM task. This observation corroborates previous studies indicating hippocampal persistent firing during the maintenance phase [4, 5, 6, 3]. However, in the present study, applying GPFA to multi-unit activity during a one-second level resolution of the WM task revealed that the NT in low-dimensional space presented a memory-load dependency between the encoding and retrieval phases, denoted as $\|g_{GR}\|$ (Figure 3). These findings support the association of the hippocampus with WM processing.

Our analysis focused on putative CA1 regions (Figure 4) in order to enhance the validity of recording site and the true positive rate of SWR detection. This criterion is supported by accumulated evidence. For instance, SWRs synchronize with spike bursts of interneuron and pyramidal neuron [44, 45, 46, 47], potentially within a $50 \mu\text{m}$ radius of the recording site [48]. Additionally, we identified increased incidence of SWRs during the first 0–400 ms of the retrieval phase (Figure 4D). This finding aligns with previous reports of heightened SWR occurrence preceding spontaneous verbal recall [22, 23], extending our understanding to a triggered retrieval condition. Moreover, the log-normal distributions of both SWR duration and ripple band peak amplitude observed in this study (Figure 4C & E) coincide with the consensus in this field [38]. Therefore, these results support the electrode placement and detected SWRs in this study. One could argue that the NT distance increase from O during SWRs (Figure 5) may be artificially inflated

towards higher values due to channel selection using UMAP clustering on spike counts. However, this potential bias does not affect the direction of NT, the memory-load dependency, nor the WM task dependency identified in this study.

Interestingly, during the retrieval phase, NT directions alternated between encoding and retrieval states during both baseline and SWR periods in a task-dependent manner (Figure 6C & D). Additionally, the balance of this fluctuation transitioned from encoding to retrieval state during SWR events (Figure 6 E & F). These results align with previous studies on the role of SWR in memory retrieval [22, 23]. Our findings suggest that (i) neuronal oscillation between encoding and retrieval states occurs during a WM task and (ii) SWR events serve as indicators of the transition in hippocampal neural states from encoding to retrieval during a WM task.

Moreover, our study noted differences specific to the WM-task type between encoding- and retrieval-SWRs (Figure 6E–F). Notably, opposing movements of encoding-SWR (eSWR) and retrieval-SWR (rSWR) were not observed in Match IN task but were apparent in Mismatch OUT task. Memory engram theory [49] might explain these observations: Match In task presented participants with previously shown letters, while Mismatch OUT task introduced a new letter absent in the encoding phase. This explanation underscores the significant role of SWR in human cognitive processes.

In conclusion, this study illustrates that during a WM task in humans, hippocampal activity fluctuate between encoding and retrieval states, uniquely transitioning from encoding to retrieval during SWR events. These findings offer novel insights into the neural correlates and functionality of working memory within the hippocampus.

Data Availability Statement

The data is available on G-Node (<https://doi.gin.g-node.org/10.12751/g-node.d76994/>). The source code is available on GitHub (<https://github.com/yanagisawa-lab/hippocampal-neural-fluctuations-during-a-WM-task-in-humans>).

References

- [1] W. B. Scoville, B. Milner, LOSS OF RECENT MEMORY AFTER BI-LATERAL HIPPOCAMPAL LESIONS, *Journal of Neurology, Neurosurgery, and Psychiatry* 20 (1) (1957) 11–21.
URL <https://www.ncbi.nlm.nih.gov/pmc/articles/PMC497229/>
- [2] L. R. Squire, The Legacy of Patient H.M. for Neuroscience, *Neuron* 61 (1) (2009) 6–9. doi:10.1016/j.neuron.2008.12.023.
URL <https://www.ncbi.nlm.nih.gov/pmc/articles/PMC2649674/>
- [3] E. Boran, T. Fedele, P. Klaver, P. Hilfiker, L. Stieglitz, T. Grunwald, J. Sarnthein, Persistent hippocampal neural firing and hippocampal-cortical coupling predict verbal working memory load, *Science Advances* 5 (3) (2019) eaav3687. doi:10.1126/sciadv.aav3687.
URL <https://www.science.org/doi/10.1126/sciadv.aav3687>
- [4] J. Kamiński, S. Sullivan, J. M. Chung, I. B. Ross, A. N. Mamelak, U. Rutishauser, Persistently active neurons in human medial frontal and medial temporal lobe support working memory, *Nature Neuroscience* 20 (4) (2017) 590–601, number: 4 Publisher: Nature Publishing Group. doi:10.1038/nn.4509.
URL <https://www.nature.com/articles/nn.4509>
- [5] S. Kornblith, R. Q. Quiroga, C. Koch, I. Fried, F. Mormann, Persistent Single-Neuron Activity during Working Memory in the Human Medial Temporal Lobe, *Current Biology* 27 (7) (2017) 1026–1032, publisher: Elsevier. doi:10.1016/j.cub.2017.02.013.
URL [https://www.cell.com/current-biology/abstract/S0960-9822\(17\)30149-5](https://www.cell.com/current-biology/abstract/S0960-9822(17)30149-5)
- [6] M. C. M. Faraut, A. A. Carlson, S. Sullivan, O. Tudusciuc, I. Ross, C. M. Reed, J. M. Chung, A. N. Mamelak, U. Rutishauser, Dataset of human medial temporal lobe single neuron activity during declarative memory

- encoding and recognition, *Scientific Data* 5 (1) (2018) 180010, number: 1 Publisher: Nature Publishing Group. doi:10.1038/sdata.2018.10. URL <https://www.nature.com/articles/sdata201810>
- [7] A. A. Borders, C. Ranganath, A. P. Yonelinas, The hippocampus supports high-precision binding in visual working memory, *Hippocampus* 32 (3) (2022) 217–230. doi:10.1002/hipo.23401.
- [8] J. Li, D. Cao, S. Yu, X. Xiao, L. Imbach, L. Stieglitz, J. Sarnthein, T. Jiang, Functional specialization and interaction in the amygdala-hippocampus circuit during working memory processing, *Nature Communications* 14 (1) (2023) 2921, number: 1 Publisher: Nature Publishing Group. doi:10.1038/s41467-023-38571-w.
URL <https://www.nature.com/articles/s41467-023-38571-w>
- [9] V. Dimakopoulos, P. Mégevand, L. H. Stieglitz, L. Imbach, J. Sarnthein, Information flows from hippocampus to auditory cortex during replay of verbal working memory items, *eLife* 11 (2022) e78677, publisher: eLife Sciences Publications, Ltd. doi:10.7554/eLife.78677.
URL <https://doi.org/10.7554/eLife.78677>
- [10] D. J. Foster, M. A. Wilson, Reverse replay of behavioural sequences in hippocampal place cells during the awake state, *Nature* 440 (7084) (2006) 680–683, publisher: Nature Publishing Group. doi:10.1038/nature04587.
URL <https://www.nature.com/articles/nature04587>
- [11] M. P. Karlsson, L. M. Frank, Awake replay of remote experiences in the hippocampus, *Nature Neuroscience* 12 (7) (2009) 913–918, publisher: Nature Publishing Group. doi:10.1038/nn.2344.
URL <https://www.nature.com/articles/nn.2344>
- [12] M. F. Carr, S. P. Jadhav, L. M. Frank, Hippocampal replay in the awake state: a potential substrate for memory consolidation and retrieval, Na-

- ture Neuroscience 14 (2) (2011) 147–153. doi:10.1038/nn.2732.
URL <https://www.nature.com/articles/nn.2732>
- [13] B. E. Pfeiffer, D. J. Foster, Hippocampal place-cell sequences depict future paths to remembered goals, Nature 497 (7447) (2013) 74–79. doi:10.1038/nature12112.
- [14] G. Girardeau, K. Benchenane, S. I. Wiener, G. Buzsáki, M. B. Zugardo, Selective suppression of hippocampal ripples impairs spatial memory, Nature Neuroscience 12 (10) (2009) 1222–1223. doi:10.1038/nn.2384.
URL <http://www.nature.com/articles/nn.2384>
- [15] S. P. Jadhav, C. Kemere, P. W. German, L. M. Frank, Awake Hippocampal Sharp-Wave Ripples Support Spatial Memory, Science 336 (6087) (2012) 1454–1458, publisher: American Association for the Advancement of Science. doi:10.1126/science.1217230.
URL <https://www.science.org/doi/abs/10.1126/science.1217230>
- [16] A. C. Singer, M. F. Carr, M. P. Karlsson, L. M. Frank, Hippocampal SWR activity predicts correct decisions during the initial learning of an alternation task, Neuron 77 (6) (2013) 1163–1173. doi:10.1016/j.neuron.2013.01.027.
- [17] A. Fernández-Ruiz, A. Oliva, E. Fermino de Oliveira, F. Rocha-Almeida, D. Tingley, G. Buzsáki, Long-duration hippocampal sharp wave ripples improve memory, Science (New York, N.Y.) 364 (6445) (2019) 1082–1086. doi:10.1126/science.aax0758.
- [18] T. Sasaki, V. C. Piatti, E. Hwaun, S. Ahmadi, J. E. Lisman, S. Leutgeb, J. K. Leutgeb, Dentate network activity is necessary for spatial working memory by supporting CA3 sharp-wave ripple generation and prospective firing of CA3 neurons, Nature Neuroscience 21 (2) (2018) 258–269, publisher: Nature Publishing Group. doi:10.1038/

s41593-017-0061-5.

URL <https://www.nature.com/articles/s41593-017-0061-5>

- [19] M. Tamura, T. J. Spellman, A. M. Rosen, J. A. Gogos, J. A. Gordon, Hippocampal-prefrontal theta-gamma coupling during performance of a spatial working memory task, *Nature Communications* 8 (1) (2017) 2182, publisher: Nature Publishing Group. doi:10.1038/s41467-017-02108-9.
URL <https://www.nature.com/articles/s41467-017-02108-9>
- [20] J. Daume, J. Kamiński, A. G. P. Schjetnan, Y. Salimpour, U. Khan, M. Kyzar, C. M. Reed, W. S. Anderson, T. A. Valiante, A. N. Mamelak, U. Rutishauser, Control of working memory by phase-amplitude coupling of human hippocampal neurons, *Nature* 629 (8011) (2024) 393–401. doi:10.1038/s41586-024-07309-z.
URL <https://www.nature.com/articles/s41586-024-07309-z>
- [21] C.-T. Wu, D. Haggerty, C. Kemere, D. Ji, Hippocampal awake replay in fear memory retrieval, *Nature Neuroscience* 20 (4) (2017) 571–580. doi:10.1038/nn.4507.
- [22] Y. Norman, E. M. Yeagle, S. Khuvis, M. Harel, A. D. Mehta, R. Malach, Hippocampal sharp-wave ripples linked to visual episodic recollection in humans, *Science* 365 (6454) (2019) eaax1030. doi:10.1126/science.aax1030.
URL <https://www.science.org/lookup/doi/10.1126/science.aax1030>
- [23] Y. Norman, O. Raccah, S. Liu, J. Parvizi, R. Malach, Hippocampal ripples and their coordinated dialogue with the default mode network during recent and remote recollection, *Neuron* 109 (17) (2021) 2767–2780.e5, publisher: Elsevier. doi:10.1016/j.neuron.2021.06.020.
URL [https://www.cell.com/neuron/abstract/S0896-6273\(21\)00461-X](https://www.cell.com/neuron/abstract/S0896-6273(21)00461-X)

- [24] Y. Watanabe, M. Okada, Y. Ikegaya, Towards threshold invariance in defining hippocampal ripples, *Journal of Neural Engineering* 18 (6) (2021) 066012. doi:10.1088/1741-2552/ac3266.
 URL <https://dx.doi.org/10.1088/1741-2552/ac3266>
- [25] E. Boran, T. Fedele, A. Steiner, P. Hilfiker, L. Stieglitz, T. Grunwald, J. Sarnthein, Dataset of human medial temporal lobe neurons, scalp and intracranial EEG during a verbal working memory task, *Scientific Data* 7 (1) (2020) 30, number: 1 Publisher: Nature Publishing Group. doi:10.1038/s41597-020-0364-3.
 URL <https://www.nature.com/articles/s41597-020-0364-3>
- [26] H. Zhang, P. D. Rich, A. K. Lee, T. O. Sharpee, Hippocampal spatial representations exhibit a hyperbolic geometry that expands with experience, *Nature Neuroscience* (Dec. 2022). doi:10.1038/s41593-022-01212-4.
 URL <https://www.nature.com/articles/s41593-022-01212-4>
- [27] R. J. Gardner, E. Hermansen, M. Pachitariu, Y. Burak, N. A. Baas, B. A. Dunn, M.-B. Moser, E. I. Moser, Toroidal topology of population activity in grid cells, *Nature* 602 (7895) (2022) 123–128, number: 7895 Publisher: Nature Publishing Group. doi:10.1038/s41586-021-04268-7.
 URL <https://www.nature.com/articles/s41586-021-04268-7>
- [28] B. M. Yu, J. P. Cunningham, G. Santhanam, S. I. Ryu, K. V. Shenoy, M. Sahani, Gaussian-Process Factor Analysis for Low-Dimensional Single-Trial Analysis of Neural Population Activity, *Journal of Neurophysiology* 102 (1) (2009) 614–635. doi:10.1152/jn.90941.2008.
 URL <https://www.ncbi.nlm.nih.gov/pmc/articles/PMC2712272/>
- [29] M. M. Churchland, B. M. Yu, J. P. Cunningham, L. P. Sugrue, M. R. Cohen, G. S. Corrado, W. T. Newsome, A. M. Clark, P. Hosseini, B. B. Scott, D. C. Bradley, M. A. Smith, A. Kohn, J. A. Movshon, K. M.

- Armstrong, T. Moore, S. W. Chang, L. H. Snyder, S. G. Lisberger, N. J. Priebe, I. M. Finn, D. Ferster, S. I. Ryu, G. Santhanam, M. Sahani, K. V. Shenoy, Stimulus onset quenches neural variability: a widespread cortical phenomenon, *Nature neuroscience* 13 (3) (2010) 369–378. doi: 10.1038/nn.2501.
URL <https://www.ncbi.nlm.nih.gov/pmc/articles/PMC2828350/>
- [30] D. Lin, M. P. Boyle, P. Dollar, H. Lee, E. S. Lein, P. Perona, D. J. Anderson, Functional identification of an aggression locus in the mouse hypothalamus, *Nature* 470 (7333) (2011) 221–226, publisher: Nature Publishing Group. doi:10.1038/nature09736.
URL <https://www.nature.com/articles/nature09736>
- [31] M. Churchland, J. Cunningham, M. Kaufman, J. Foster, P. Nuyujukian, S. Ryu, K. Shenoy, Neural population dynamics during reaching, *Nature* 487 (7405) (2012) 51–56. doi:10.1038/nature11129.
URL <https://www.ncbi.nlm.nih.gov/pmc/articles/PMC3393826/>
- [32] A. S. Ecker, P. Berens, R. J. Cotton, M. Subramaniyan, G. H. Denfield, C. R. Cadwell, S. M. Smirnakis, M. Bethge, A. S. Tolias, State dependence of noise correlations in macaque primary visual cortex, *Neuron* 82 (1) (2014) 235–248. doi:10.1016/j.neuron.2014.02.006.
URL <https://www.ncbi.nlm.nih.gov/pmc/articles/PMC3990250/>
- [33] J. C. Kao, P. Nuyujukian, S. I. Ryu, M. M. Churchland, J. P. Cunningham, K. V. Shenoy, Single-trial dynamics of motor cortex and their applications to brain-machine interfaces, *Nature Communications* 6 (2015) 7759. doi:10.1038/ncomms8759.
- [34] J. A. Gallego, M. G. Perich, L. E. Miller, S. A. Solla, Neural Manifolds for the Control of Movement, *Neuron* 94 (5) (2017) 978–984. doi:10.1016/j.neuron.2017.05.025.
URL <https://www.sciencedirect.com/science/article/pii/S0896627317304634>

- [35] Z. Wei, H. Inagaki, N. Li, K. Svoboda, S. Druckmann, An orderly single-trial organization of population dynamics in premotor cortex predicts behavioral variability, *Nature Communications* 10 (1) (2019) 216, publisher: Nature Publishing Group. doi:10.1038/s41467-018-08141-6. URL <https://www.nature.com/articles/s41467-018-08141-6>
- [36] J. Kim, A. Joshi, L. Frank, K. Ganguly, Cortical–hippocampal coupling during manifold exploration in motor cortex, *Nature* 613 (7942) (2023) 103–110, publisher: Nature Publishing Group. doi:10.1038/s41586-022-05533-z. URL <https://www.nature.com/articles/s41586-022-05533-z>
- [37] J. Niediek, J. Boström, C. E. Elger, F. Mormann, Reliable Analysis of Single-Unit Recordings from the Human Brain under Noisy Conditions: Tracking Neurons over Hours, *PLOS ONE* 11 (12) (2016) e0166598, publisher: Public Library of Science. doi:10.1371/journal.pone.0166598. URL <https://journals.plos.org/plosone/article?id=10.1371/journal.pone.0166598>
- [38] A. A. Liu, S. Henin, S. Abbaspoor, A. Bragin, E. A. Buffalo, J. S. Farrell, D. J. Foster, L. M. Frank, T. Gedankien, J. Gotman, J. A. Guidera, K. L. Hoffman, J. Jacobs, M. J. Kahana, L. Li, Z. Liao, J. J. Lin, A. Losonczy, R. Malach, M. A. van der Meer, K. McClain, B. L. McNaughton, Y. Norman, A. Navas-Olive, L. M. de la Prida, J. W. Rueckemann, J. J. Sakon, I. Skelin, I. Soltesz, B. P. Staresina, S. A. Weiss, M. A. Wilson, K. A. Zaghloul, M. Zugardo, G. Buzsáki, A consensus statement on detection of hippocampal sharp wave ripples and differentiation from other fast oscillations, *Nature Communications* 13 (1) (2022) 6000, number: 1 Publisher: Nature Publishing Group. doi:10.1038/s41467-022-33536-x. URL <https://www.nature.com/articles/s41467-022-33536-x>
- [39] K. Kay, M. Sosa, J. E. Chung, M. P. Karlsson, M. C. Larkin, L. M.

- Frank, A hippocampal network for spatial coding during immobility and sleep, *Nature* 531 (7593) (2016) 185–190. doi:10.1038/nature17144.
- [40] G. Buzsáki, Hippocampal sharp wave-ripple: A cognitive biomarker for episodic memory and planning, *Hippocampus* 25 (10) (2015) 1073–1188, _eprint: <https://onlinelibrary.wiley.com/doi/pdf/10.1002/hipo.22488>. doi:<https://doi.org/10.1002/hipo.22488>
URL <https://onlinelibrary.wiley.com/doi/abs/10.1002/hipo.22488>
- [41] L. McInnes, J. Healy, N. Saul, L. Großberger, UMAP: Uniform Manifold Approximation and Projection, *Journal of Open Source Software* 3 (29) (2018) 861. doi:10.21105/joss.00861.
URL <https://joss.theoj.org/papers/10.21105/joss.00861>
- [42] P. J. Rousseeuw, Silhouettes: A graphical aid to the interpretation and validation of cluster analysis, *Journal of Computational and Applied Mathematics* 20 (1987) 53–65. doi:10.1016/0377-0427(87)90125-7.
URL <https://www.sciencedirect.com/science/article/pii/0377042787901257>
- [43] P. Virtanen, R. Gommers, T. E. Oliphant, M. Haberland, T. Reddy, D. Cournapeau, E. Burovski, P. Peterson, W. Weckesser, J. Bright, S. J. van der Walt, M. Brett, J. Wilson, K. J. Millman, N. Mayorov, A. R. J. Nelson, E. Jones, R. Kern, E. Larson, C. J. Carey, Polat, Y. Feng, E. W. Moore, J. VanderPlas, D. Laxalde, J. Perktold, R. Cimrman, I. Henriksen, E. A. Quintero, C. R. Harris, A. M. Archibald, A. H. Ribeiro, F. Pedregosa, P. van Mulbregt, SciPy 1.0 Contributors, SciPy 1.0: fundamental algorithms for scientific computing in Python, *Nature Methods* 17 (2020) 261–272, aDS Bibcode: 2020NatMe..17..261V. doi:10.1038/s41592-019-0686-2.
URL <https://ui.adsabs.harvard.edu/abs/2020NatMe..17..261V>
- [44] G. Buzsáki, Two-stage model of memory trace formation: a role for

- "noisy" brain states, *Neuroscience* 31 (3) (1989) 551–570. doi:10.1016/0306-4522(89)90423-5.
- [45] M. L. V. Quyen, A. Bragin, R. Staba, B. Crépon, C. L. Wilson, J. Engel, Cell Type-Specific Firing during Ripple Oscillations in the Hippocampal Formation of Humans, *Journal of Neuroscience* 28 (24) (2008) 6104–6110, publisher: Society for Neuroscience Section: Brief Communications. doi:10.1523/JNEUROSCI.0437-08.2008.
URL <https://www.jneurosci.org/content/28/24/6104>
- [46] S. Royer, B. V. Zemelman, A. Losonczy, J. Kim, F. Chance, J. C. Magee, G. Buzsáki, Control of timing, rate and bursts of hippocampal place cells by dendritic and somatic inhibition, *Nature Neuroscience* 15 (5) (2012) 769–775, number: 5 Publisher: Nature Publishing Group. doi:10.1038/nn.3077.
URL <https://www.nature.com/articles/nn.3077>
- [47] N. Hájos, M. R. Karlócai, B. Németh, I. Ulbert, H. Monyer, G. Szabó, F. Erdélyi, T. F. Freund, A. I. Gulyás, Input-output features of anatomically identified CA3 neurons during hippocampal sharp wave/ripple oscillation in vitro, *The Journal of Neuroscience: The Official Journal of the Society for Neuroscience* 33 (28) (2013) 11677–11691. doi:10.1523/JNEUROSCI.5729-12.2013.
- [48] E. W. Schomburg, C. A. Anastassiou, G. Buzsáki, C. Koch, The Spiking Component of Oscillatory Extracellular Potentials in the Rat Hippocampus, *The Journal of Neuroscience* 32 (34) (2012) 11798–11811. doi:10.1523/JNEUROSCI.0656-12.2012.
URL <https://www.ncbi.nlm.nih.gov/pmc/articles/PMC3459239/>
- [49] X. Liu, S. Ramirez, P. T. Pang, C. B. Puryear, A. Govindarajan, K. Deisseroth, S. Tonegawa, Optogenetic stimulation of a hippocampal engram activates fear memory recall, *Nature* 484 (7394) (2012) 381–385, number:

7394 Publisher: Nature Publishing Group. doi:10.1038/nature11028.
URL <https://www.nature.com/articles/nature11028>

Ethics Declarations

All study participants provided their written informed consent, subsequent to the approval from the pertinent institutional ethics review board (Kantonale Ethikkommission Zürich, PB 2016–02055).

Author Contributions

Y.W. and T.Y. conceptualized the study; Y.W. performed the data analysis; Y.W. and T.Y. wrote the original draft; and all authors reviewed the final manuscript.

Acknowledgments

This research was funded by a grant from the Exploratory Research for Advanced Technology (JPMJER1801).

Declaration of Interests

The authors declare that they have no competing interests.

Inclusion and Diversity Statement

We support inclusive, diverse, and equitable conduct of research.

Declaration of Generative AI in Scientific Writing

The authors employed ChatGPT, provided by OpenAI, for enhancing the manuscript's English language quality. After incorporating the suggested improvements, the authors meticulously revised the content. Ultimate responsibility for the final content of this publication rests entirely with the authors.

Tables

Subject ID	# of sessions	AHL	AHR	PHL	PHR	ECL	ECR	AL	AR	
1	4	✓	n.a.	✓	✓	✓	✓	n.a.	✓	n.a.
2	7	✓	✓	✓	✓	✓	✓	✓	✓	AH
3	3	✓	✓	✓	✓	✓	✓	✓	✓	AI
4	2	✓	✓	✓	✓	✓	✓	✓	✓	AHL & AI
5	3	✓	n.a.	n.a.	✓	n.a.	n.a.	✓	n.a.	
6	6	✓	✓	✓	✓	✓	✓	✓	✓	AHL & P
7	4	✓	✓	✓	✓	✓	✓	✓	✓	AI
8	5	✓	✓	✓	✓	✓	✓	✓	✓	
9	2	✓	✓	✓	✓	✓	✓	✓	✓	E

Table 1 – Electrode Distribution within the Dataset

This figure denotes the placements of electrodes and seizure onset zones. Regions marked with ✓ were included in the dataset, while those imprinted with n.a. were absent. The abbreviations used are as follows: AHL, left hippocampal head; AHR, right hippocampal head; PHL, left hippocampal body; PHR, right hippocampal body; ECL, left entorhinal cortex; ECR, right entorhinal cortex; AL, left amygdala; AR, right amygdala; SOZ represents the seizure onset zone.

Subject	AHL	AHR	PHL	PHR
1	0.60 ± 0.14	n.a.	n.a.	0.1 ± 0
2	0.21 ± 0.16	0.17 ± 0.21	0.18 ± 0.22	0.20 ± 0.15
3	0.40 ± 0.42	0.83 ± 0.12	n.a.	n.a.
4	0.10 ± 0.00	0.10 ± 0.00	0.90 ± 0.00	0.10 ± 0.14
5	n.a.	n.a.	n.a.	n.a.
6	0.63 ± 0.06	n.a.	n.a.	0.27 ± 0.06
7	0.10 ± 0.00	0.35 ± 0.35	0.37 ± 0.47	0.10 ± 0.00
8	0.13 ± 0.10	n.a.	0.28 ± 0.49	n.a.
9	n.a.	0.85 ± 0.07	0.15 ± 0.07	n.a.

Table 2 – Silhouette Score of UMAP Clustering for SWR⁺ Candidates and SWR⁻ Candidates

The silhouette scores (mean ±SD across sessions per subject) for UMAP clustering of SWR⁺ candidates and SWR⁻ candidates are based on their respective multi-unit spike patterns (Figure 4A). The mean scores were 0.205 and the standard deviation was 0.285, calculated for the interquartile range (IQR; Figure 4B).

Subject ID	# of sessions	# of trials	ROI	# of SWRs	SWR incidence [Hz]
#1	2	100	AHL	274	0.34
#3	2	97	AHR	325	0.42
#4	2	99	PHL	202	0.26
#6	2	100	AHL	297	0.37
#9	2	97	AHR	72	0.09
Total = 10		Total = 493		Total = 1170	0.30 ± 0.13 (mean ± SD)

Table 3 – Summary of Detected SWRs

The table provides statistics of presumptive CA1 regions and SWR events. Only the initial two sessions (sessions 1 and 2) from each subject were included in our analysis to reduce sampling bias.

Figures

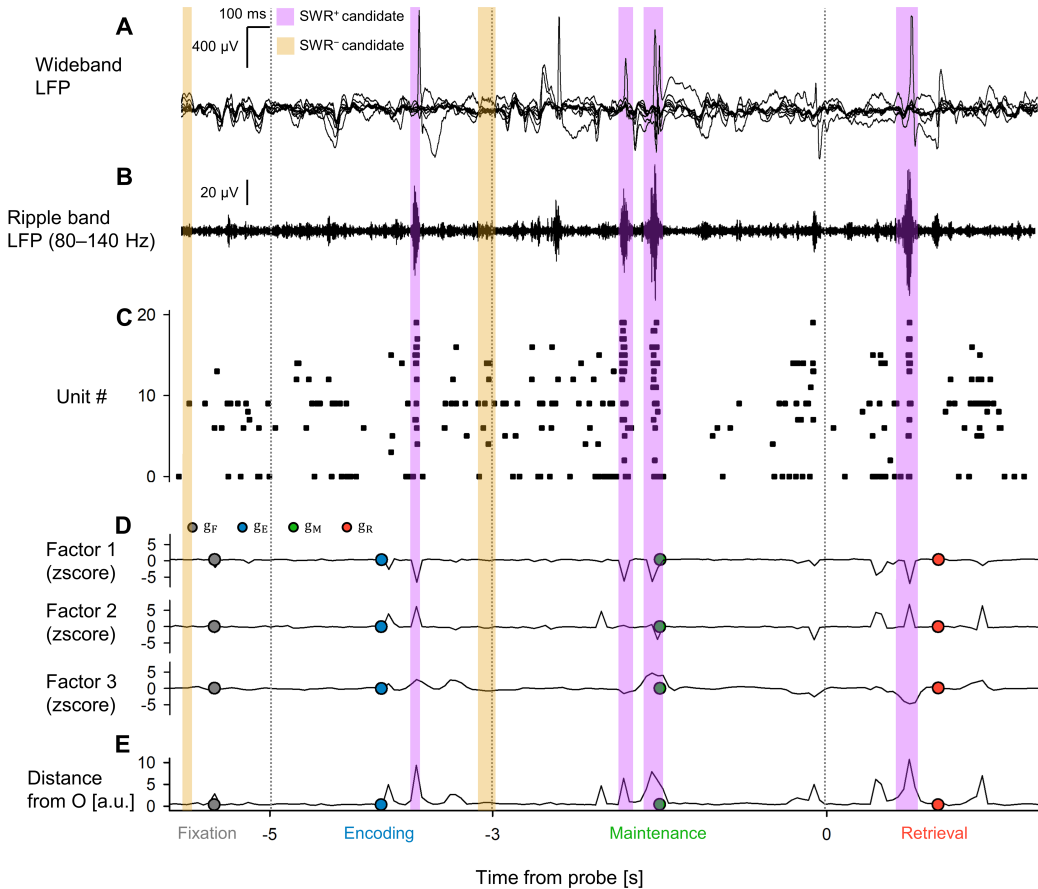


Figure 1 – Local Field Potentials, Multiunit Activity, and Neural Trajectories in the Hippocampus During a Modified Sternberg Task

A. Representative wideband LFP signals for intracranial EEG recording from the left hippocampal head are presented. This recording took place while the subject performed a modified Sternberg working memory task. Task stages included fixation (1 s, gray), encoding (2 s, blue), maintenance (3 s, green), and retrieval (2 s, red). **B.** Displays the associated ripple band LFP traces. Note purple and yellow rectangles, which denote the timings for SWR⁺ candidates and SWR⁻ candidates, respectively (the latter serving as control events for SWR⁺). **C.** A raster plot illustrates multi-unit spikes from the LFP traces. These spikes have been sorted using a spike algorithm [37]. **D.** Shows neural trajectories (NTs) computed by GPFA[28] based on spike counts per unit with 50-ms bins. The geometric median of each phase is marked by dot circles. **E.** Indicates the distance of the NT from the origin point O .

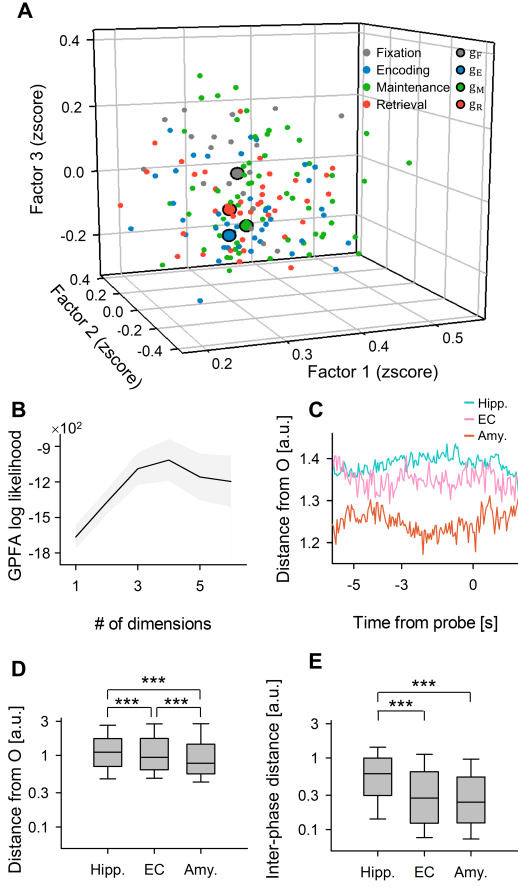


Figure 2 – State-Dependent Neural Trajectory of Hippocampal Neurons

A. Neural trajectories (NTs) depicted as a point cloud within the first three-dimensional factors derived from GPFA [28]. The smaller dots represent 50-ms NT bins, and the larger dots with *black* edges denote the geometric medians for each phase in the Sternberg working memory task: fixation ($\|g_F\|$, *gray*), encoding ($\|g_E\|$, *blue*), maintenance ($\|g_M\|$, *green*), and retrieval ($\|g_R\|$, *red*). **B.** The figure presents the log-likelihood of the GPFA models versus the number of dimensions used to embed multi-unit spikes found in the medial temporal lobe (MTL) regions. Specifically, the elbow method identified three as the optimal dimension. **C.** This panel displays the distance of the NTs from the origin (O) for the hippocampus (Hipp.), entorhinal cortex (EC), and amygdala (Amy.), plotted against the time elapsed from the probe onset. **D.** The NT distance from O within the MTL regions is shown. The hippocampus has the greatest distance, followed by the EC and the Amygdala. **E.** The box plot illustrates inter-phase NT distances within the MTL regions.

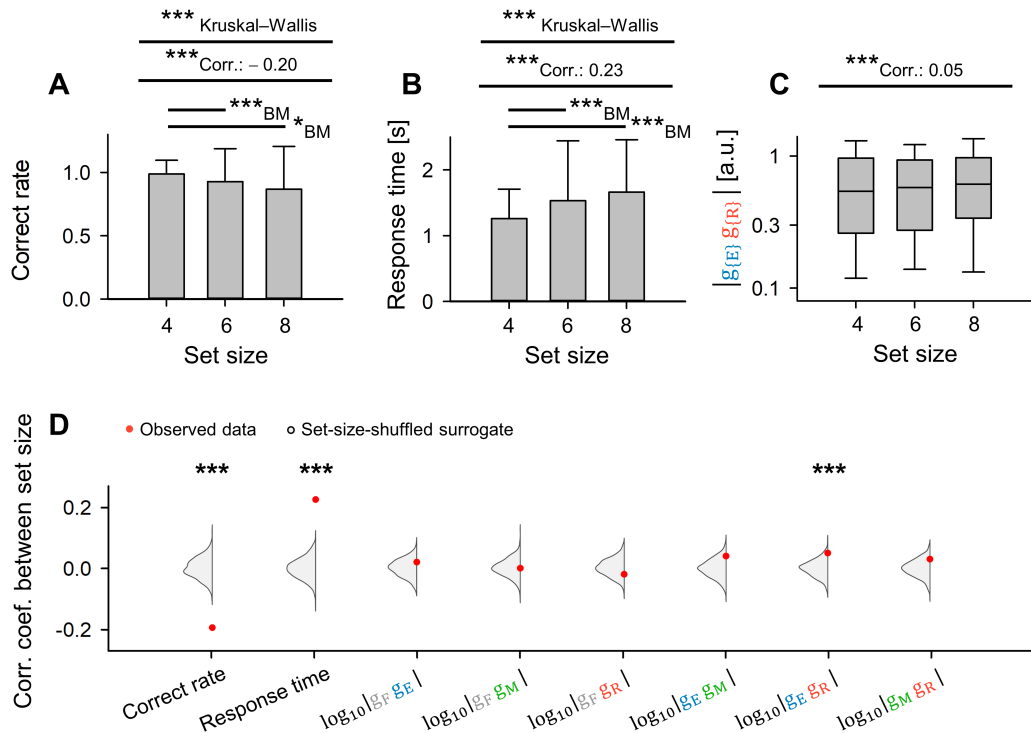


Figure 3 – Positive Correlation between Memory Load and Neural Trajectory Distance in the Hippocampus between Encoding and Retrieval Phases

A. The relationship between set size (number of letters to be encoded) and accuracy in the working memory task (coefficient = -0.20 , $***p < 0.001$). **B.** The correlation between set size and response time (coefficient = 0.23 , $***p < 0.001$). **C.** The correlation between set size on the inter-phase distances between the encoding and retrieval phases ($\|g_{[E}g_{[R}]\|$) (correlation coefficient = 0.05 , $***p < 0.001$). **D.** Experimental observations of correlations between set size and the following parameters: accuracy, response time, $\log_{10}\|g_{[F}g_{[E}]\|$, $\log_{10}\|g_{[F}g_{[M}]\|$, $\log_{10}\|g_{[F}g_{[R}]\|$, $\log_{10}\|g_{[E}g_{[M}]\|$, $\log_{10}\|g_{[E}g_{[R}]\|$, and $\log_{10}\|g_{[M}g_{[R}]\|$ represented by red dots. The kernel density plots (gray) illustrate the corresponding shuffled surrogate with set size ($n = 1,000$) ($***ps < 0.001$).

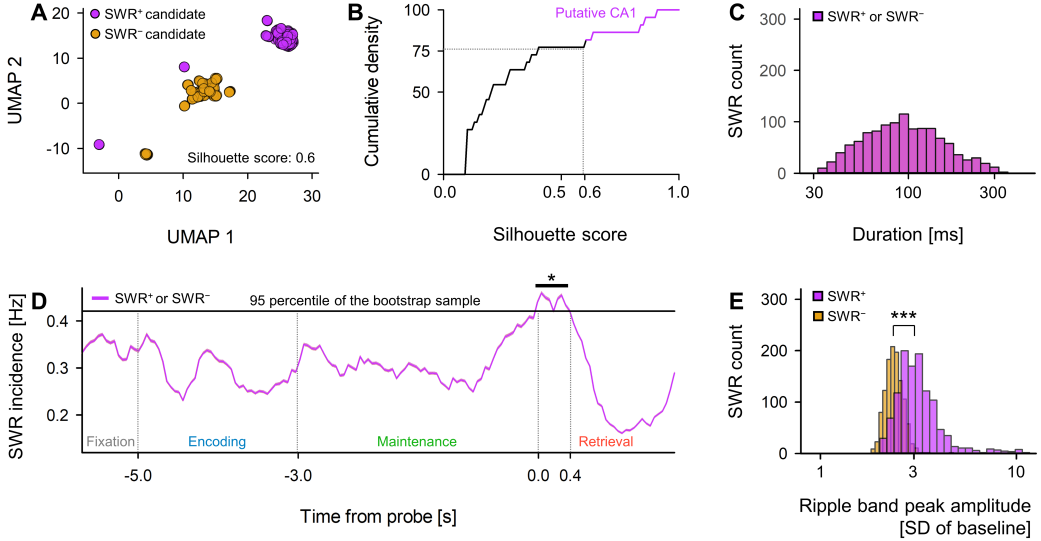


Figure 4 – Detection of SWRs in Putative CA1 Regions

A. Two-dimensional UMAP [41] projection displays multi-unit spikes during SWR⁺ candidates (*purple*) and SWR⁻ candidates (*yellow*). **B.** A cumulative density plot indicates silhouette scores, reflecting UMAP clustering quality (see Table 2). Hippocampal regions with silhouette scores exceeding 0.60 (equivalent to the 75th percentile) are identified as putative CA1 regions. SWR⁺ and SWR⁻ candidates, which were recorded from these regions, are classified as SWR⁺ and SWR⁻ respectively ($n_s = 1,170$). **C.** Identical distributions of SWR⁺ (*purple*) and SWR⁻ (*yellow*) distributions, based on their definitions (93.0 [65.4] ms, median [IQR]). Note that these distributions exhibit log-normality. **D.** Identical SWR incidence for both SWR⁺ (*purple*) and SWR⁻ (*yellow*), relative to the probe's timing (mean \pm 95% confidence interval). However, 95% confidence interval may not be visibly apparent due to their narrow ranges. Note that a significant SWR incidence increase was detected during the initial 400 ms of the retrieval phase (0.421 [Hz], * $p < 0.05$, bootstrap test). **E.** Distributions of ripple band peak amplitudes for SWR⁻ (*yellow*; 2.37 [0.33] SD of baseline, median [IQR]) and SWR⁺ (*purple*; 3.05 [0.85] SD of baseline, median [IQR]) are manifested (** $p < 0.001$, the Brunner–Munzel test). Note the log-normality for SWR⁺ events.

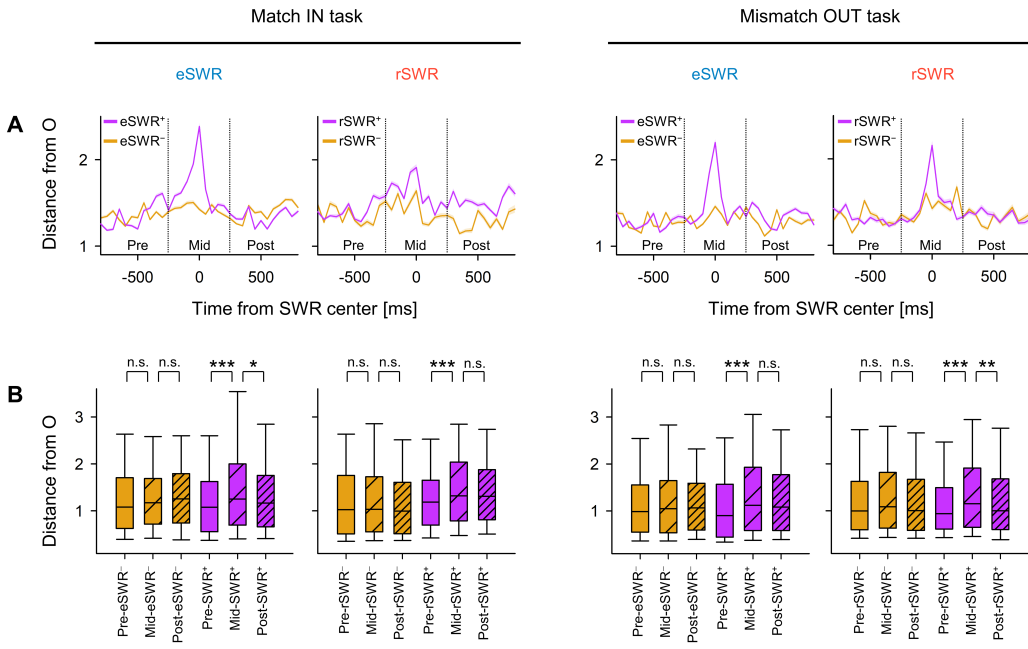


Figure 5 – Transient Change in Neural Trajectory during SWR

A. The distance from origin (O) of the peri-sharp-wave-ripple neural trajectory (mean $\pm 95\%$ confidence interval). The intervals may be obscured due to their minimal ranges. **B.** The distance from the origin (O) during the pre-, mid-, and post-SWR periods is demonstrated (* $p < 0.05$, ** $p < 0.01$, *** $p < 0.001$; Brunner–Munzel test applied). Abbreviations: SWR, sharp-wave ripple events; eSWR, SWR during the encoding phase; rSWR, SWR within the retrieval phase; SWR⁺, positive SWR event; SWR⁻, control events for SWR⁺; pre-, mid-, or post-SWR refer to the time intervals from -800 to -250 ms, from -250 to $+250$ ms, or from $+250$ to $+800$ ms, respectively, all relative to the SWR center.

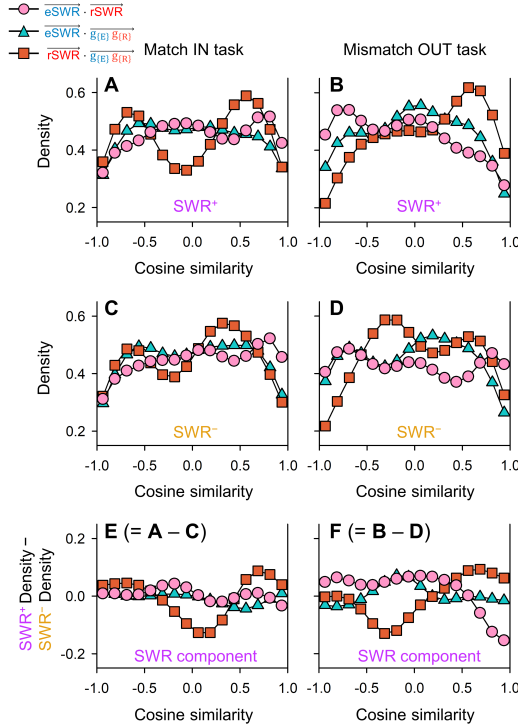


Figure 6 – Direction of Neural Trajectory During SWR Based on Encoding and Retrieval States

A–B The kernel density estimation distributions of $\overrightarrow{\text{eSWR}}^+ \cdot \overrightarrow{\text{rSWR}}^+$ (pink circles), $\overrightarrow{\text{eSWR}}^+ \cdot \overrightarrow{\text{g}_{[\text{E}]}} \overrightarrow{\text{g}_{[\text{R}]}}$ (blue triangles), and $\overrightarrow{\text{rSWR}}^+ \cdot \overrightarrow{\text{g}_{[\text{E}]}} \overrightarrow{\text{g}_{[\text{R}]}}$ (red rectangles) in Match In (*A*) and Mismatch OUT tasks (*B*). **C–D** The corresponding distributions of SWR^- instead of those of SWR^+ in *A* and *B*. **E–F** The differences in the distributions of SWR^+ and those of SWR^- , showing SWR components ($E = C - A$ & $F = D - B$). Biphasic distributions of $\overrightarrow{\text{rSWR}}^- \cdot \overrightarrow{\text{g}_{[\text{E}]}}$ indicate fluctuations between the encoding and retrieval states during the Sternberg task. Also, contradicting directionality between $\overrightarrow{\text{eSWR}}^+$ and $\overrightarrow{\text{rSWR}}^+$ was observed (pink circles) not in Match IN task (**E**), but in Mismatch OUT task (**F**). Lastly, transitions from the retrieval to encoding states are evident in the SWR components in both Match IN and Mismatch OUT tasks (red rectangles in *E–F*).